PAPER • OPEN ACCESS

Patient-specific Monte Carlo-based organ dose estimates in spiral CT via optical 3D body scanning and adaptation of a voxelized phantom dataset: proof-of-principle

To cite this article: Francesca Saveria Maddaloni *et al* 2023 *Phys. Med. Biol.* **68** 084002

IOP Publishing Phys. Med. Biol. 68 (2023) 084002 https://doi.org/10.1088/1361-6560/acc37d

Physics in Medicine & Biology

IPEM Institute of Physics and Engineering in Medicine

OPEN ACCESS

RECEIVED
29 October 2022

REVISED
21 February 2023

ACCEPTED FOR PUBLICATION
10 March 2023

PUBLISHED
4 April 2023

PAPER

Patient-specific Monte Carlo-based organ dose estimates in spiral CT via optical 3D body scanning and adaptation of a voxelized phantom dataset: proof-of-principle

Francesca Saveria Maddaloni[1,2,5], **Antonio Sarno**[1,2,5], **Giovanni Mettivier**[1,2], **Stefania Clemente**[3], **Caterina Oliviero**[3], **Roberta Ricciardi**[2,4], **Antonio Varallo**[2,4] and **Paolo Russo**[1,2,*]

[1] Dipartimento di Fisica 'Ettore Pancini', Università di Napoli Federico II, I-80126 Napoli, Italy
[2] INFN Sezione di Napoli, I-80126 Napoli, Italy
[3] Azienda Ospedaliera Universitaria Federico II, I-80131 Napoli, Italy
[4] Scuola di Specializzazione in Fisica Medica, Università di Napoli Federico II, I-80131 Napoli, Italy
[5] These authors contributed equally to this work.
[*] Author to whom any correspondence should be addressed.

E-mail: russo@na.infn.it

Keywords: CT dosimetry, voxelized phantoms, Monte Carlo simulations, organ doses, Geant4, 3D scanner

Supplementary material for this article is available online

Abstract

Objective. We present a method for personalized organ dose estimates obtained before the computed tomography (CT) exam, via 3D optical body scanning and Monte Carlo (MC) simulations. *Approach*. A voxelized phantom is derived by adapting a reference phantom to the body size and shape measured with a portable 3D optical scanner, which returns the 3D silhouette of the patient. This was used as an external rigid envelope for incorporating a tailored version of the internal body anatomy derived from a phantom dataset (National Cancer Institute, NIH, USA) matched for gender, age, weight, and height. The proof-of-principle was conducted on adult head phantoms. The Geant4 MC code provided estimates of the organ doses from 3D absorbed dose maps in the voxelized body phantom. *Main results*. We applied this approach for head CT scanning using an anthropomorphic voxelized head phantom derived from 3D optical scans of manikins. We compared the estimates of head organ doses with those provided by the NCICT 3.0 software (NCI, NIH, USA). Head organ doses differed up to 38% using the proposed personalized estimate and MC code, with respect to corresponding estimates calculated for the standard (non-personalized) reference head phantom. Preliminary application of the MC code to chest CT scans is shown. Real-time pre-exam personalized CT dosimetry is envisaged with adoption of a Graphics Processing Unit-based fast MC code. *Significance*. The developed procedure for personalized organ dose estimates before the CT exam, introduces a new approach for realistic description of size and shape of patients via voxelized phantoms specific for each patient.

1. Introduction

Estimation of radiation dose from radiological procedures in patients is a fundamental requirement for the related assessment of radiation exposure in the population. A recent report (based on the NCRP report 184, NCRP 2019) investigates this issue in the United States population for the period 2006–2016, showing that 74 million computed tomography (CT) scans in 2016 determined an average individual effective dose of 1.37 mSv, out of a total effective dose of 2.2 mSv from all radiologic and nuclear medicine procedures (Mettler *et al* 2020), so representing about 62% of the total individual dose burden. At the same time, it has been noted that the per capita dose decreased by nearly 20% over this period (Einstein 2020). In all cases, this outlines the importance of patient-based radiation dose monitoring for patient risk assessment, in particular for CT exams (Tsalafoutas *et al* 2020).

Patient dose estimates in CT via simulation software (Damilakis 2021) require both an appropriate *in silico* replication of the scanner and a refined computational model of the patient anatomy. Monte Carlo (MC) simulations of the scanner geometry and scan protocol include a description of the actual x-ray beam spectrum and conformation as shaped by the filter and bowtie compensator (Turner *et al* 2009, 2010). Usually, digital anatomical models for patient dose estimates represent an 'average' (reference) patient (e.g. Papadakis and Damilakis 2022), but recently, large patient's model datasets have been produced for better representng the gender variability. Based on the scanner CT computational model and on a digital patient model, conversion coefficients for dose estimates from measurable values are computed via MC simulations (ICRP 2007, Martin *et al* 2020).

The organ and effective dose to the patient undergoing CT examination depend both on the scanner type and protocol and on the physical conformation of the body (size and shape), e.g. as based on size-specific dose estimates and water-equivalent diameter (AAPM 2011, 2019a, 2019b, Abuhaimed and Martin 2020). In principle, dose estimates could be derived for all the scanner types and protocols, with *in silico* simulations (e.g. Li *et al* 2011, Fujii *et al* 2020). On the other hand, a digital patient cohort large enough to represent closely all possible patient anatomies, is unrealistic: hence, effective dose or organ dose estimates completely tailored to the actual patient under examination are not practical.

To mitigate this limitation, a proposed approach is to tune and deform pre-calculated reference digital patient models (Zvereva *et al* 2017, Borbinha *et al* 2019), e.g. based on patient's weight and height (Sahbaee *et al* 2014, Lee *et al* 2015, 2019, ICRP 2020). In the approach of Lee *et al* (2019), conventional digital phantoms were deformed starting from secondary body parameters such as sitting height, head height, length, and breadth, sagittal abdominal diameter. Upper arm, waist, buttock, thigh, and calf circumferences were used for extending the patient cohort, also including 10th, 50th and 90th percentile standing heights and body weights of adult male and female Caucasian populations. In a different approach, the user interface application developed by NCI in USA (Lee *et al* 2015) permits the customization of the patient model starting from the weight and height of the patient, for the calculation of effective dose from a pre-calculated datasheet which includes the description of many different reference persons. In any case, the proposed customized digital phantoms are models of the exposed patient derived from epidemiological and statistical data, and they do not present the shape and silhouette of any actual patient under CT examination.

In this work, we propose a method for the customization of patient digital models based on the assessment of the external shape of the actual patient, for a customized phantom description of the individual patient, for input to a MC simulation of the CT scan for dose estimates. This might represent a more accurate approach to consider the effective anatomy of the patient, for minimization of patient dose assessment inaccuracy, with respect to present patient size metrics, in particular for pediatric patients (Sapignoli *et al* 2022). To this purpose, a new methodology and a new MC code was developed, for organ dose estimates using the patient-specific voxelized phantom. Such an approach relies on a pre-acquisition of the external shape of the patient via a 3D body scanner. Having determined in this way the patient's silhouette, the standard body model (digital phantom from a reference person dataset, selected appropriately for gender and class age) undergoes a deformation to fit the measured shape.

We point out that, while it is possible to derive a patient-specific voxelized phantom *after* the CT scan by segmentation of the corresponding CT slices, our goal is to provide a method for personalized CT organ dose estimates *before the exam*, by combining the 3D optical scan of the patient body, by creating a personalized (voxel) phantom and by executing a (fast) MC simulation for organ dose estimate, reproducing the characteristic of the CT scan protocol and the patient anatomy. This estimate could be used to tune the CT patient dose before the scan, to be compared with dose estimates using conventional CT dose estimates which adopt standard reference person phantoms (e.g. as provided by ICRP Publication 110, 2009, or by ICRP Publication 145, 2020). As a result, any discrepancy between the two organ dose estimates could be evidenced, to be possibly attributed to the specific description of the patient anatomy with respect to reference person-based dose estimates.

Here we present the new method, validate the MC program, and evaluate, via MC dose estimates, the impact of the customization of the patient model (assembled from the measured body silhouette) on the estimated dose, in the case of head CT scanning. We also point out that our main goal in this work is to outline the entire method, to present and validate a MC code for organ dose estimate, and to investigate the feasibility of the proposed approach, rather than providing optimized solutions for each of its application steps. For example, the dosimetric method here investigated could be adopted with a different MC simulation code, or with a different optical scan technique, or with different and more efficient methods for phantom volume deformation than the rigid deformation approach here adopted. Moreover, the case of head CT scan was chosen, as a first approach for a proof-of-principle of the proposed method to pre-exam personalized CT dosimetry. The cross-sectional area of the head region showed variations of $\pm 6\%$ for male patients and $\pm 7\%$ for female patients (Huda *et al* 2004). CT dosimetry for more complex anatomies (e.g. chest) are under investigation (though preliminary addressed in the following) and will be reported in the next steps of this initial study.

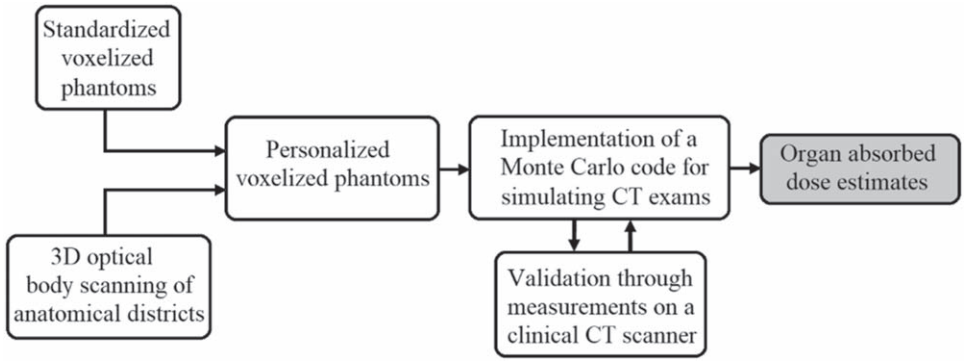

Figure 1. Flowchart showing the process for obtaining personalized organ dose estimates via validated MC simulations, using digital voxel phantoms basically derived from a reference dataset and personalized though 3D optical scans of the patient silhouette.

2. Method

The flowchart in figure 1 describes the methodology steps proposed for the personalized MC estimate of organ doses; the processing steps are described in the following sections.

2.1. The MC simulation

The Monte Carlo code was derived from a previous version used for *in silico* x-ray breast imaging investigations (di Franco *et al* 2020, Sarno *et al* 2017a, 2018, 2022). It is based on the Geant4 toolkit and physics list Option4. The new code version permits to perform spiral scanning geometry and to set the beam aperture at the detector, the length of the scan and the pitch. The MC software includes simulation of photoelectric, Compton and Rayleigh x-ray photon interactions. The electrons are not tracked but supposed to deposit energy locally. For the purpose of this work, the patient dose map was simulated: for each interacting event, the location and the released energy was computed and stored in a 3D matrix.

2.2. The beam model

The replicated scanner specifications and characteristics, adopted for this proof-of-principle study, were those of the Astelion CT scanner produced by Toshiba (model CGS-61A). The scanner permitted the use of tube voltages of 80 kV, 100 kV, 120 kV and 135 kV. To replicate the model of the x-ray beam in the MC simulations, we followed the approach described in Turner *et al* (2009). This permits to measure the relative beam fluence without precise knowledge of the shape of the bowtie embodied on the scanner. With this goal, a 3 cm^3 Radcal 20 $\times$ 6–3CT ionization chamber was placed at the center of the field of view (FOV) and the dependence of the beam intensity on the distance from the isocenter was investigated. The accuracy of the dosimeter was within $\pm$4%, as reported in the calibration certificate. The axis of the ionization chamber was placed corresponding to the axis of the CT gantry and laterally centered. During the measurements, the x-ray source was kept stationary (scout image). Several measurements were performed with the ionization chamber moved far from the scanner isocenter along the radial direction of the gantry in the plane perpendicular to the beam propagation direction. The relative beam intensity was sampled with a sampling step of 1 cm up to 14 cm distance from the scanner isocenter. The evaluated beam profile was used in the MC simulations to describe the probability density function of the directions of the generated photons. On the other hand, in the axial direction, the beam was supposed to emit photons with a uniform probability. To model the x-ray spectra, the beam HVL was evaluated (Turner *et al* 2009) and the used spectra computed as suggested in Hernandez *et al* (2017); then, the measured HVL was matched by varying the added aluminum filtration. X-ray spectra were modelled for 80 kV, 100 kV, 120 kV and 135 kV tube voltages (i.e., all the spectra available from the used Astelion CT scanner).

2.3. The customized digital phantom

Customized phantoms were generated starting from the family of digital phantoms developed by the USA National Institute of Health (NCICT phantoms, Geyer *et al* 2014, Lee *et al* 2015). The dataset includes 370 phantoms of both genders and of various heights and weights and representative of a large range of patient ages, from newborns to adult individuals. Specifically, in this work we used one digital phantom from the dataset representing an adult male, and one representing an adult female individual. The first comprised 769 axial slices whose thickness was 2.207 mm; each slice comprised a matrix of 267 $\times$ 194 pixels, with pixel size of 1.579 mm $\times$ 1.579 mm. The female phantom comprised 610 axial slices with thickness of 2.700 mm and made

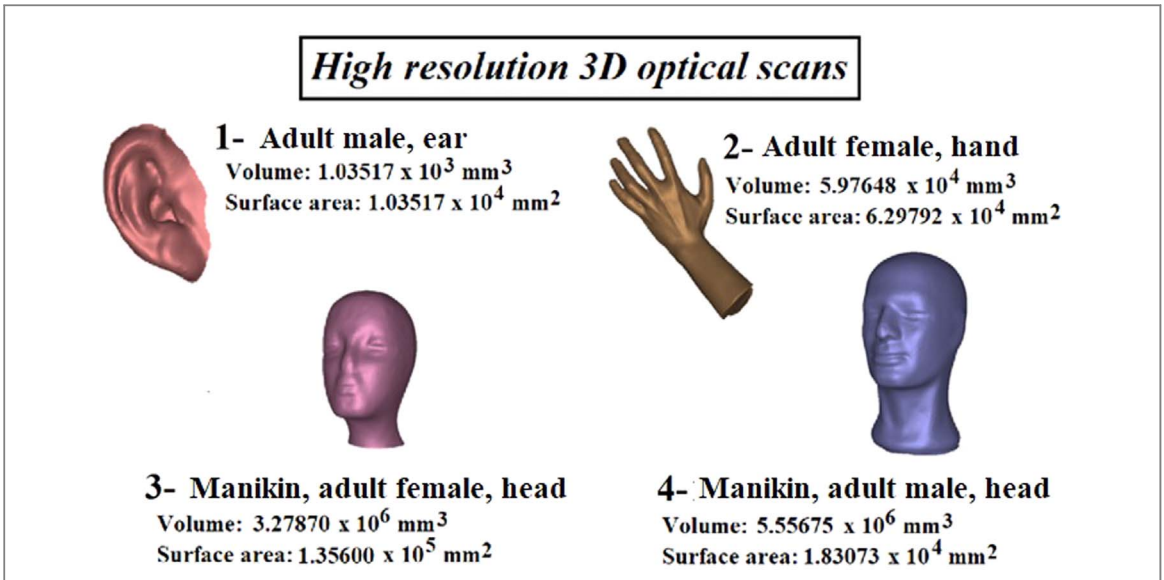

Figure 2. 3D volume rendering of example 3D optical scans of human subjects' organs (1–2) and polystyrene commercial manikins (3–4), obtained with the optical scanner. From each scan we derived the volume (mm^3) and outer surface area (mm^2) of the corresponding voxelized phantom, indicated in the figure. 1—adult male ear; 2—adult female hand; 3—adult male manikin; 4—adult female manikin. Repeated scans (by one operator) of the manikinsshowed a resolution in the order of 10 ppm and a repeatability of about 1.2% for volume and surface measurements.

by a matrix of 308 × 240 pixels with pitch of 1.260 mm. In this work, exclusively head scanning protocols were investigated and exclusively the heads of the two phantoms were employed.

To reproduce a digital phantom with the dimensions of the actual patient, we adapted the selected phantom to the silhouette derived from an optical 3D scan. Hence, an optical 3D scan of the actual patient *physical phantom* was acquired; then, the male or female digital phantom selected from the NCI database underwent a rigid adaptation, which consisted either of compressing or stretching the voxel sizes, to reduce the discrepancy between the dimension to the 3D patient rendering. In this proof-of-principle laboratory-based study, we used polystyrene manikins instead of actual patients, for the evaluation of the methods and of the impact of the model mismatch to the actual patient on the estimated dose. The silhouette of the manikin was acquired via the hand-held Artec Eva 3D scanner (https://www.artec3d.com/it/portable-3d-scanners/artec-eva). This can be used to obtain an accurate and pre-textured 3D model of medium-sized objects, such as a human head or torso.

The Artec Eva 3D optical scanner works by structured light triangulation, that allows to receive 3D data from objects contactless, and by simply illuminating them with (unharmful) light flashes. It uses two cameras, mounted at different locations. For acquiring surface data via the active structured light technique, it is necessary to project pre-defined patterns on the surface of the object (usually in the form of parallel beams): the patterns become then distorted when projected onto the object's surface (the scanner captures these images using the cameras). Then, this information is given to the software that elaborates it via the method of triangulation to calculate the object's depth and surface information. The final output from the scanner is a digital 3D representation on the computer.

A structured-light 3D scanner can only take 3D images of what the cameras can see: therefore, to create a digital model of the entire object, optical scans must be taken at multiple angles (typically by rotating around the object). The scans are then cleaned up, merged, and stitched together (known as post-processing) to create a complete digital model (the user receives a color texturized 3D mesh made up of triangles). The Artec Eva 3D scanner was controlled by a notebook running the Artec Studio Professional ver. 16 software, used for reconstructions and elaborations of the models. Artec Studio performs the fusion of all the frames acquired during the rotation of the scanner and allows the user to 'correct' the 3D model, for example, by filling holes, erase undesired parts of the object etc. Figure 2 shows the 3D rendering of the 3D scans of body parts and manikins.

To evaluate alternative approaches for dose estimates for patients whose silhouette differs from the standard one, we have also employed the NCICT 3.0 software (NCI, NIH, USA) (Lee *et al* 2015). This software permits to customize the patient model on the basis of his/her height and weight; hence, both for female and male adult models and fixed heights, we tested the influence on the dose calculation of changing the phantom size by increasing at maximum its weight, this change being supposed to correspond to the maximum difference in the patient silhoutte and dimension.

2.4. Dose computations

The absorbed dose (D) to the kth organ (D_k) was computed as the average dose over the organ tissue volume as follows:

$$D_k = \frac{\sum_i E_i}{m_k}, \tag{1}$$

where m_k is the mass of the kth organ tissue, and the sum considers the energy deposited (E_i) for each of the ith interacting events occurring in the kth organ. Electrons are supposed to release energy locally and de-excitation processes are not simulated. With the intent of passing from the simulated dose to the patient model to dose released by the clinical scanner with a selected protocol, the CF factors were introduced (Ding *et al* 2015). These were computed as the ratio:

$$CF = \frac{\mathrm{CTDI}^{\mathrm{air}}_{100,\mathrm{m}}}{\mathrm{CTDI}^{\mathrm{air}}_{100,\mathrm{s}}}, \tag{2}$$

where CTDI_{100} is the CT dose index evaluated for a 100 mm long pencil ion-chamber. The superscript air indicates that it is evaluated at the scanner isocenter with the ion-chamber placed in air (with no phantoms). The subscripts 'm' and 's' indicate measured and simulated CTDI_{100}, respectively. The simulated value is expressed in mGy per photon, while the measured one was evaluated for 1 mAs. The CF factor permits to convert dose to the digital model (in mSv per photon) to dose to the actual represented patient, in mSv per mAs. In order to calculate the CT dose index in the simulated scanner ($\mathrm{CTDI}^{\mathrm{air}}_{100,\mathrm{s}}$), we modelled the pencil ion-chamber as a cylinder made of dry air whose diameter was 1.10 mm and the length was 100 mm:

$$\mathrm{CTDI}^{\mathrm{air}}_{100,\mathrm{s}} = \frac{1}{N_{\mathrm{ev}}} \frac{E_{\mathrm{i}}}{m_{\mathrm{i}}} \frac{100}{NT}, \tag{3}$$

where m_{i} is the mass of the air contained in the ion-chamber volume, N_{ev} is the total number of generated primary photons (10^9 in our case), N the number of image sections irradiated in the single source rotation, and T is the width of the image sections (in cm). For this evaluation, the source was confined to an axial scan. $\mathrm{CTDI}^{\mathrm{air}}_{100,\mathrm{s}}$ was measured on the clinical scanner with the same geometrical and protocol used for the simulated scan, and for 100 mAs.

To validate the MC code, we also computed and measured the $\mathrm{CTDI}_{\mathrm{w}}$. For this reason, the pencil ion-chamber was first placed along the central axis of a PMMA cylinder with a diameter of 16 cm and the axis of 10 cm as used in the evaluation, for the CTDI in the head examinations (AAPM 2019b). The $\mathrm{CTDI}_{100,\mathrm{s}}$ at the center of the phantom ($\mathrm{CTDI}_{100,\mathrm{s,c}}$) was computed as indicated in equation (3) for the case in air. Similar simulations were performed shifting the ion-chamber 15 cm laterally from the axis of the PMMA phantom. The simulations were repeated for the ion-chamber located at 3, 6, 9 and 12 o'clock positions over the circular perimeter of the PMMA cylinder (AAPM 2019b) and the simulated weighted CTDI ($\mathrm{CTDI}_{\mathrm{w,s}}$) was evaluated. Measurements for the same simulated geometry were repeated on the clinical scanner, and the $\mathrm{CTDI}_{\mathrm{w,m}}$ was evaluated.

2.5. Monte Carlo validation

To validate the new scanning geometry of the CT scanner used, and the specific beam conformation, we performed additional tests. A first simple test was performed to confirm that the simulated beam profile reflected that of the measured one. Secondly, the measured $\mathrm{CTDI}_{\mathrm{w}}$ to CTDI_{100} ratio was compared to the simulated one at 80 kV, 100 kV, 120 kV and 135 kV tube voltage.

A physical male adult head phantom was 3D printed statring form the digital one from the NCI database (figure 3). The head digital phantom was digitally cut via a freeware CAD software (3D Builder, Microsoft Corporation Inc.) in 4 sections so to obtain 4 STL format files. These 4 sections were separately given as input to the 3D printing slicing software (Cura, Ultimaker) which returned a *gcode* format file used for the operations in the printing process. The physical phantom was manufactured via Ultimaker 2 fused deposition modelling (FDM) 3D printing technology. The phantom was made with white PLA material and printed through a 0.4 mm diameter nozzle, layer height of 0.2 mm, and infill factor of 40%. The printing time spent for each section of the phantom was about 18 h.

To measure the dose distribution, a large area of 20 cm × 25 cm GafChromic™ film piece of XR-QA2 type (Ashland Inc., USA) was then placed in a coronal plane between two halves of the phantom. The phantom was then scanned at 120 kV, 300 mA, pitch 1 and beam aperture 16 × 1. The GafChromic™ film lot was previously calibrated as described in previous works (Tomic *et al* 2010, Di Lillo *et al* 2016, Sarno *et al* 2017b, Valero *et al* 2022). For this reason, 3 cm × 5 cm film pieces were irradiated at known exposure levels. They were held by a PMMA frame and nylon wires and faced the x-ray source (figure 4(a)).

They were irradiated via scout acquisitions whose length permitted to include the entire piece in the field. A 6 cm^3 RadCal ion chamber model 10 × 6–06 was then located at the same position of the GafChromic™ sheets

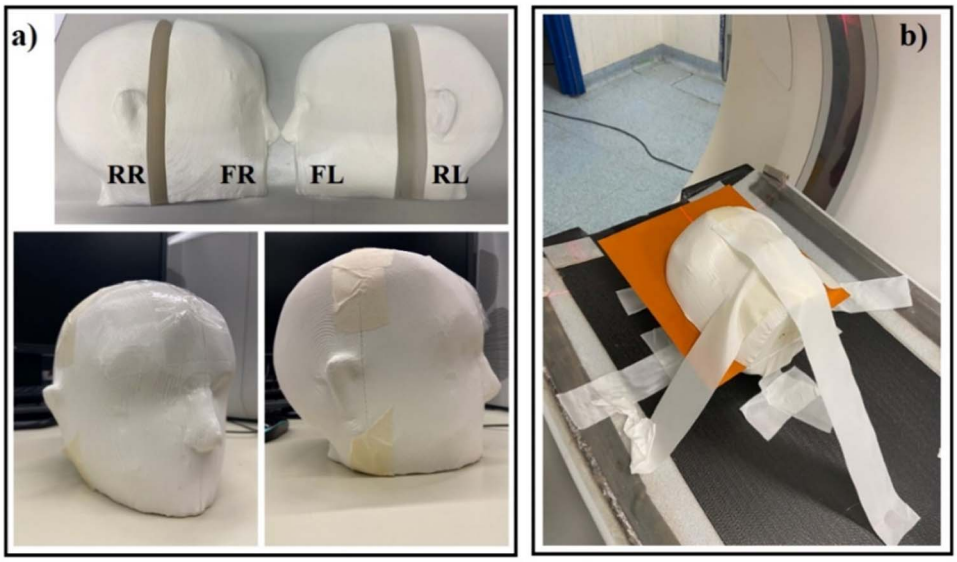

Figure 3. (a) Front and side photos of the 3D printed male head phantom made of PLA, composed of four parts (front left FL, front right FR, rear left RL, rear right RR) printed separately with a 40% infill factor. Paper tape was used for joining all parts in place. The corresponding digital phantom was derived from a voxelized adult male head phantom of the NCI dataset. (b) 3D printed head phantom placed on the patient couch in the CT scanner field of view: the photo shows a XR-QA2 radiochromic film sheet sandwiched between front and rear parts of the phantom, for recording the 2D coronal map of the absorbed dose in the CT scan.

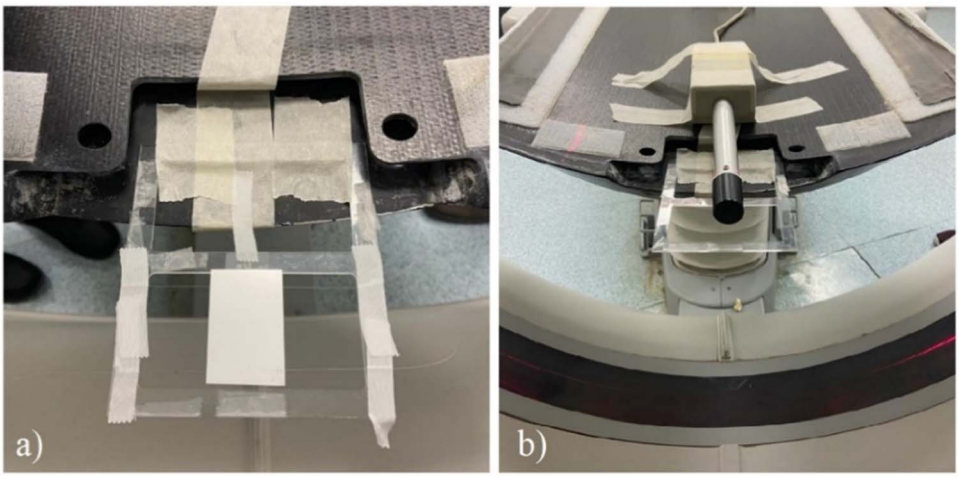

Figure 4. (a) GafChromic film sheets facing the x-ray source during the calibration of the lot; (b) ion-chamber located to measure the air-kerma at which GafChromic weas exposed.

and air kerma measured by repeating the previous scout images (figure 4(b)). The accuracy of the dosimeter was within ±4%, as reported in the calibration certificate. To increase the measured air kerma and to cover a broad enough exposure range, both radiochromic film pieces and the ion chamber underwent from 1 to 14 consecutive irradiations. To reduce the acquisition time and scanner load, we selected three contiguous regions of interest of the exposed GafChromic™ piece, meant as independent acquisitions for the evaluation of the calibration function, as done in Tomic *et al* (2010).

Figure 5(a) shows the evaluated calibration curve; this was fitted with a rational curve (Di Lillo *et al* 2016). The uncertainty curve was evaluated as described in Di Lillo *et al* (2016) and Valero *et al* (2022) and reported in figure 5(b). The dose evaluations were performed for a dose level which guaranteed a total uncertainty lower than 5% (figure 5(b)).

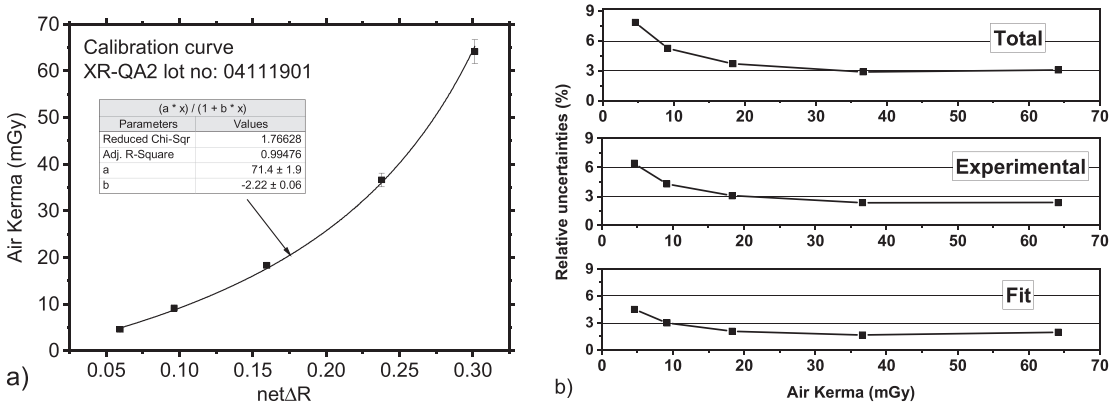

Figure 5. (a) Dose-response curve measured for the used XR-QA2 GafChromic film lot at 120 kV and (b) the corresponding uncertainty curves.

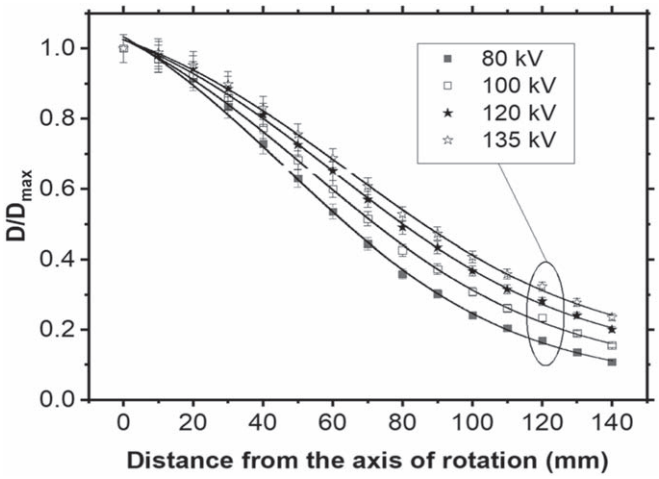

Figure 6. Beam intensity profile along the central axial plane of the CT scanner FOV, normalized to the isocenter value. Continuous lines represent sigmoid fitting curves of the measured profiles (data points).

3. Results

3.1. Beam profile model

Figure 6 shows the measured beam profiles in the radial direction in the axial plane. It was evaluated up to 14 cm from the scanner isocenter, intended to cover the entire FOV for head scanning and for tube voltages of 80 kV, 100 kV, 120 kV and 135 kV. Continuous lines represent sigmoidal fits used for simpler analytical model of the profile following the parametric formula:

$$\frac{D}{D_{\max}} = \frac{(A_1 - A_2)}{1 + \left(\frac{x}{x_0}\right)^d} + A_2. \tag{4}$$

Here, x is the distance from the isocenter and A_1, A_2, x_0 and d are fitting coefficients. Table 1 reports sigmoidal curve fitting coefficients evaluated for the measured curves in figure 6. R^2 fitting parameters are also reported in the table, showing the high suitability of the proposed sigmoidal model. The beam profiles are supposed to be symmetric with respect to the central axis of the scanner, in the CT scanner simulations. A radiochromic film sheet was irradiated at the scanner isocenter for verifying the assumption of uniform probability distribution of the beam exposure in the axial direction (figure 7).

The film was irradiated with the stationary x-ray source and attached at the gantry to be joined with the beam footprint (figure 7(c)). The exposure profile was sampled at the scanner isocenter in the axial direction (figure 7(a)) (in addition to the radial direction, figure 7(c)). A fit of the central part of the beam profile (figure 7(b)) shows that the hypothesis of beam uniformity in the axial direction is reliable. Hence, a constant

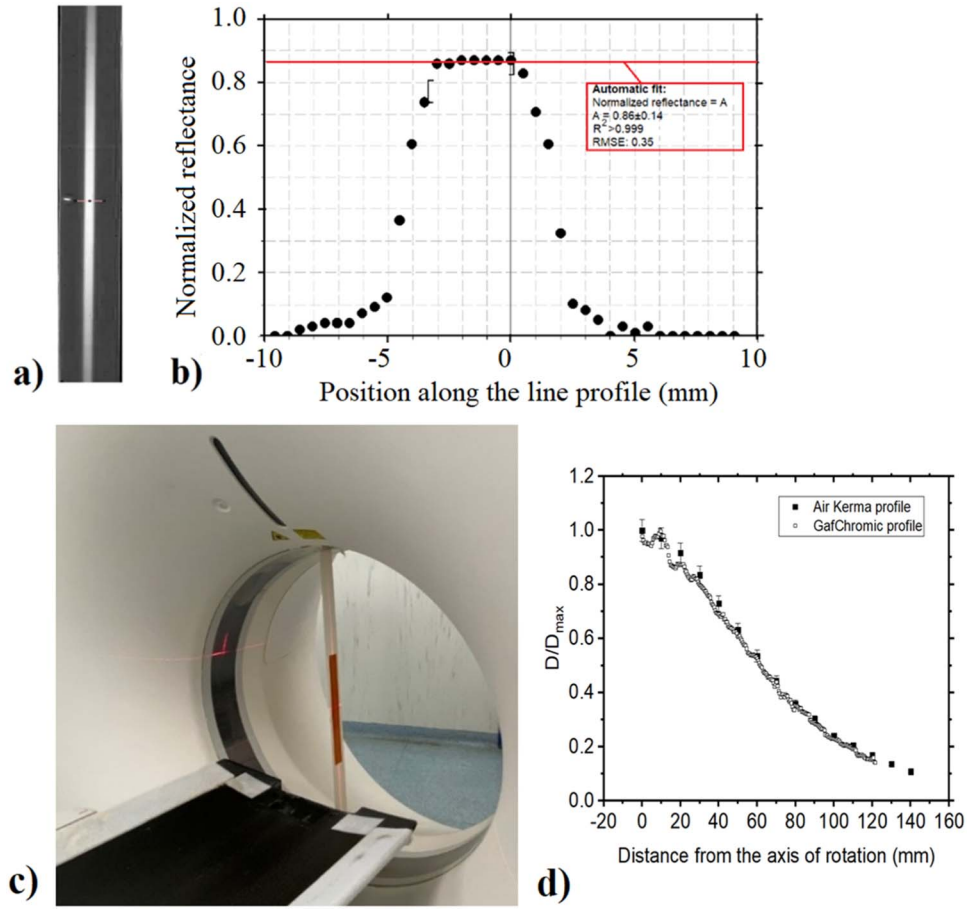

Figure 7. (a) Footprint of the beam at the scanner isocenter impressed on a calibrated GafChromic™ film and (b) beam profile along the CT longitudinal axis. (c) The beam profile was measured via a GafChromic™ film piece placed in the middle sagittal plane of the scanner FOV, stationary with the beam during the scout acquisition. (d) Example radial profile of beam output (normalized at isocenter) measured with the radiochromic film (open squares) and simulated with the Geant4 MC code (closed squares).

Table 1. Parameters of the sigmoidal fitting curves of the beam profiles in figure 6.

Tube voltage (kV)	A_1	A_2	x_0	d	R^2
80	1.27 ± 0.07	0.04 ± 0.01	47 ± 4	33 ± 3	0.998 59
100	1.23 ± 0.07	0.06 ± 0.02	54 ± 4	35 ± 3	0.998 26
120	1.19 ± 0.05	0.10 ± 0.01	61 ± 3	35 ± 3	0.998 87
135	1.18 ± 0.05	0.12 ± 0.02	65 ± 3	36 ± 3	0.998 71

function, used for fitting central profile points comprised in the 4 mm aperture of the beam, presented a R^2 fit parameter higher than 0.999. The beam profile also presents exposure tails that may be caused by the finite size of the focal spot or scatter from bowtie and collimators. These tails were not simulated. However, such an amount not comprised in the primary beam is considered in the *CF* factor thanks to the use of long ion-chamber for sensing the entire beam output in the dose computation. Figure 7(d) also shows a comparison between the simulated beam profile as a function of the distance from the isocenter, and that measured with the radiochromic film.

Table 2 reports the measured beam HVL for the available tube voltages. The evaluation was performed at the scanner isocenter and at 50 mm from the isocenter, where the bowtie could also influence the beam quality. However, differences between HVL in the two positions are within the experimental error. In this work, the beam was modelled following the HVL evaluated at the scanner isocenter.

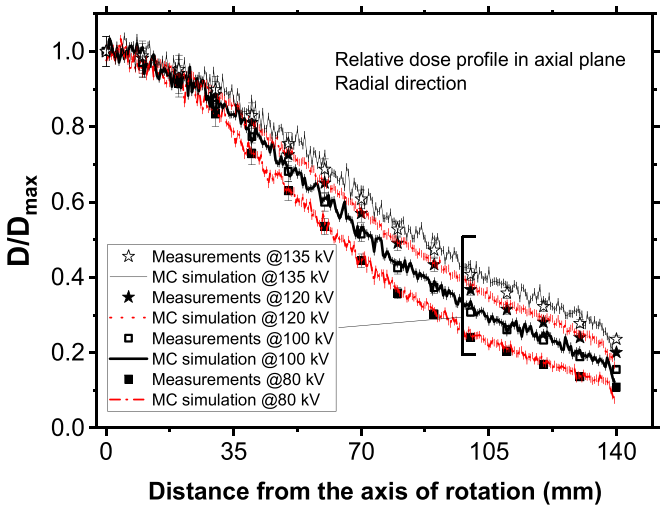

Figure 8. Measured and simulated relative beam profiles (normalized air kerma as a function of radial distance from the axis of rotation).

Table 2. Beam HVL at the scanner isocenter and at 50 mm from the scanner isocenter.

Tube voltage (kV)	HVL at the isocenter (mm Al)	HVL at 50 mm from the isocenter (mm Al)
80	3.6 ± 0.6	4.2 ± 0.5
100	4.7 ± 0.7	5.4 ± 0.6
120	6.8 ± 0.7	6.6 ± 0.6
135	7.9 ± 0.3	7.7 ± 0.9

3.2. Monte Carlo validation

3.2.1. Validation of the simulated beam profile

In the first validation test, summarized in figure 8, we compared simulated beam profiles (continuous curves) to the measured ones (data points). These beam profiles were evaluated as air kerma (normalized to the value at the isocenter) as a function of the radial distance, for tube voltages between 80 kV and 135 kV.

As in the cases of evaluations in previous paragraphs, these profiles were evaluated in the radial direction up to 140 mm from the isocenter. Simulated beam profiles, evaluated with a spatial resolution of 1 mm, lie on the measured curves (differences much less than 1%). A second test compared simulated and measured $CTDI_w$, normalized to the CTDI measured in air ($CTDI_{air}$), without using the head PMMA phantom. Results are reported in figure 9. Differences were contained within 4%, largely within the measurement's errors of the $CTDI_w/CTDI_{air}$ ratio of about 8%.

3.2.2. Validation of the simulated dose

Figure 10 shows the simulated 3D dose distribution obtained for the male (figures 10(a), (b)) and female (figures 10(c), (d)) adult NCICT head phantoms (100 kV, 10^9 histories, pitch 1). These 3D dose distributions, replicated at 120 kV, were used for MC validation tests. Hence, the same evaluation was performed via a GafChromic™ film sandwiched in between the two halves of the 3D printed head phantom. To compare dose distribution profiles, the head was simulated with a homogenous phantom made of PLA material with a density of 0.408 g cm^{-3}. This value was obtained by calculating the mean of the measured densities of the four head sections.

Figures 11(a) and (b) report the simulated and measured dose distributions in the middle plane of the head phantom, respectively. Simulated and measured axial profiles of dose distribution evaluated at the scanner isocenter are reported in figure 11(c). Simulated dose profiles were rescaled by means of the *CF* factor. Figure 11(c) shows an acceptable agreement between the measured and simulated dose levels. The spatial frequency of the quasi-sinusoidal curve (peak-to-peak frequency) was 0.068 mm^{-1} and 0.061 mm^{-1} for the simulated and measured profiles, respectively. The little difference may be ascribed to misalignments of the central plane of the phantom in the measurements. The discrepancy between consecutive peak-to-valley differences was 6.5%, in the order of the uncertainty of measured differences, which present the higher value.

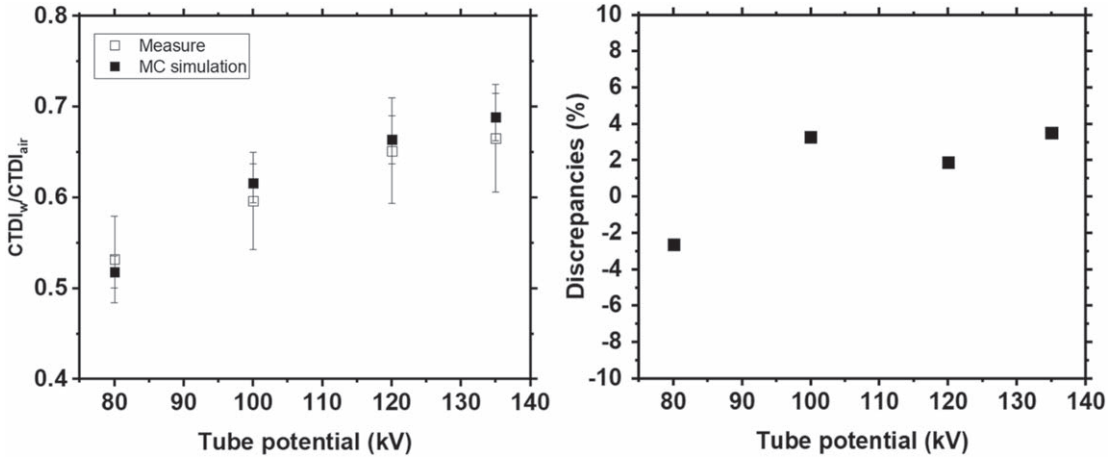

Figure 9. (a) Simulated and measured $CTDI_w$ normalized to the isocenter air kerma. (b) Percent discrepancies.

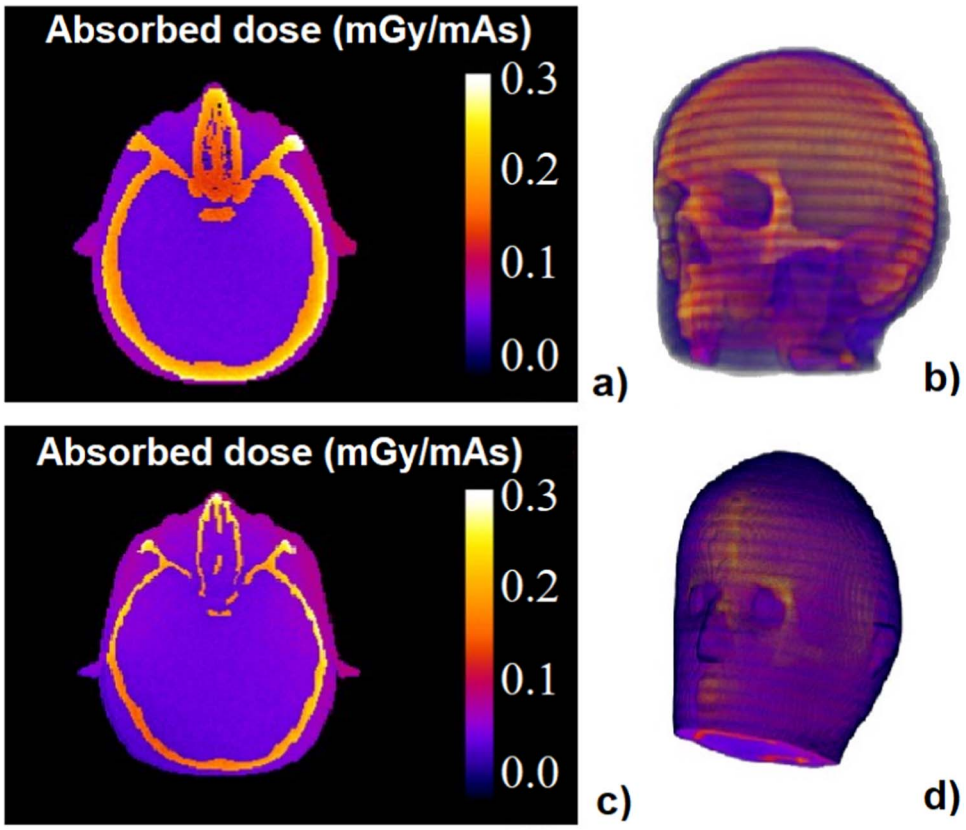

Figure 10. Central slice from the 3D dose distribution in the (a) male and (c) female adult phantom, after MC simulation at 100 kV in a spiral CT scan; (b) and (d) show corresponding 3D dose distributions.

The dose evaluated via the MC software adopted in this study and that computed via NCICT (Lee *et al* 2015) were compared, and the percentage discrepancies were reported in tables 3 and 4, for male and female phantoms, respectively. The percentage discrepancies D_f were calculated as:

$$D_f = 100 \times \frac{(\text{Dose}_{\text{NCICT}} - \text{Dose}_{\text{MC}})}{\text{Dose}_{\text{NCICT}}} \tag{5}$$

For validation purposes, we compared the dose estimated for four tissues contained in the NCI head phantoms: brain, eyeballs, eye lens and pituitary gland. Comparisons were done for all tube voltages allowed by

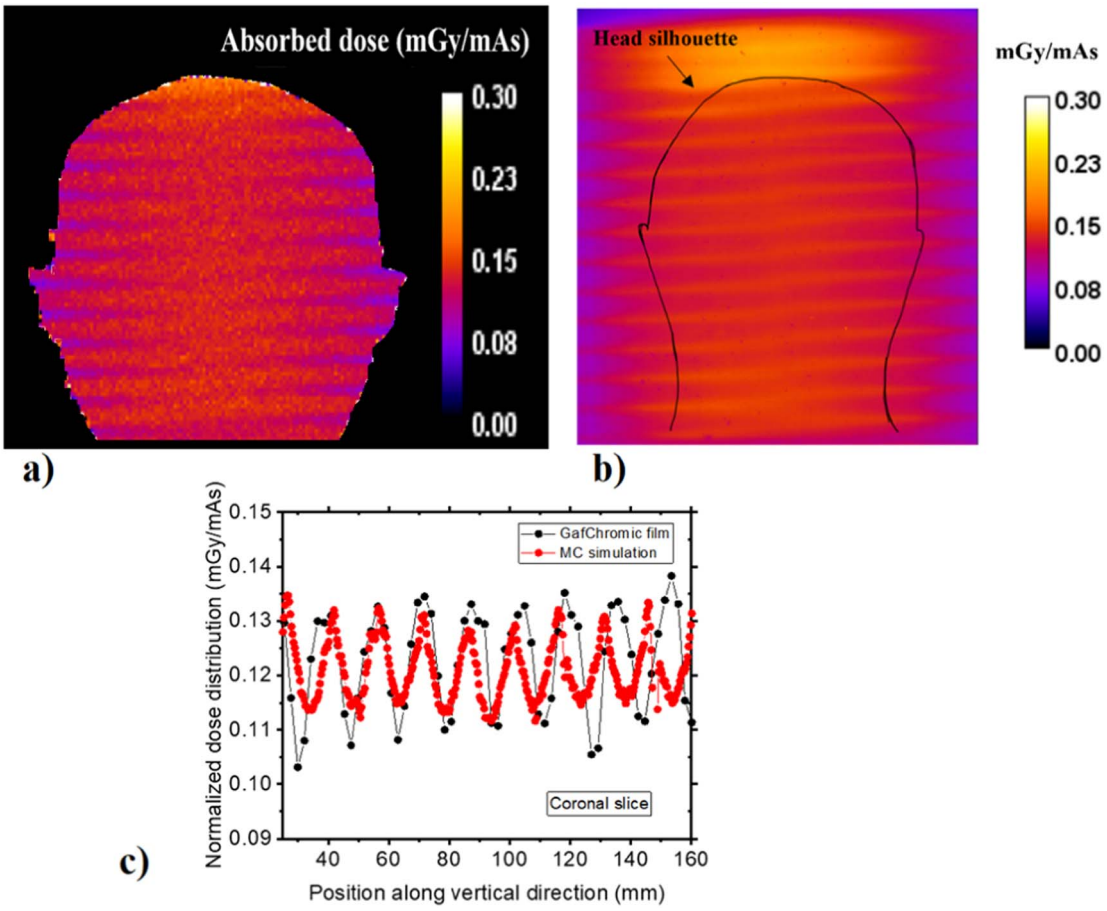

Figure 11. (a) Central slice of simulated dose distribution (120 kV spiral CT scan), and (b) measurements performed with a large area GafChromic™ film sandwiched between two halves of the printed head phantom in coronal middle plane (the head silhouette has been drawn for ease of localization). (c) Dose profiles along the scanner isocenter.

Table 3. Relative discrepancies between dose estimates via the MC software used in this work and those from NCICT for the male phantom.

Tube voltage (kV)	Brain	Eyeballs	Lens	Pituitary gland
80	+16.4	+10.2	+6.1	+23.9
100	+3.5	+0.5	−3.7	+11.7
120	−10.9	−5.9	−7.8	−3.7
135	+4.7	+11.7	+10.4	+9.6

Table 4. Relative discrepancies between dose estimates via the MC software used in this work and those from NCICT for the female phantom.

Tube voltage (kV)	Brain	Eyeballs	Lens	Pituitary gland
80	+6.8	+6.2	+6.9	−15.6
100	+11.9	+11.3	+13.4	−5.2
120	+0.02	+4.1	+8.2	−17.2
135	+15.2	+20.7	+24.8	−0.68

the considered Astelion CT apparatus (i.e., 80 kV, 100 kV, 120 kV and 135 kV) and for male (table 3) and female (table 4) adult NCI phantoms, respectively.

Maximum differences were found for the estimated dose to the pituitary gland at 80 kV in the case of the male phantom (23.9%), and for lens dose at 135 kV in the case of the female phantom (24.8%). These differences

Table 5. Evaluated *CF* factors for the used configurations.

Tube voltage (kV)	Simulation (mSv N_{ph}^{-1})	Measurement (mSv mAs^{-1})	*CF* (N_{ph} mAs^{-1})
80	2.36×10^{-13}	0.000 78	$(8.27 \pm 0.34) \times 10^{10}$
100	2.09×10^{-13}	0.0012	$(1.41 \pm 0.06) \times 10^{11}$
120	1.92×10^{-13}	0.0016	$(2.11 \pm 0.09) \times 10^{11}$
135	1.82×10^{-13}	0.0019	$(2.61 \pm 0.11) \times 10^{11}$

Table 6. Percentage organ dose discrepancies between standard and customized phantoms, male phantom.

Tube voltage (kV)	Brain	Eyeballs	Eye lens	Pituitary gland
80	+0.8	−7.4	−10.2	+4.9
100	−2.7	−9.2	−13.1	−0.7
120	−4.5	−10.0	−12.2	−4.1
135	−5.1	−9.9	−13.7	−4.9

Table 7. Percentage dose discrepancies between standard and customized phantoms, female phantom.

Tube voltage (kV)	Brain	Eyeballs	Eye lens	Pituitary gland
80	+17.9	+8.9	+4.7	+20.4
100	+36.3	+30.8	+28.2	+38.0
120	+22.2	+17.6	+14.9	+23.3
135	+24.4	+16.8	+3.0	+6.6

were mainly due to the two different MC codes employed in the simulations. Main differences may reside in the beam shape model—based on profile measurements in this work—and in the calculated conversion factors (equation (2)); a little discrepancy may also derive from subtle differences in the simulated physics. However, in most of the cases, differences were lower than 15%, in absolute value. In analysing literature data comparing different software codes used for organ dose estimates, we note that differences as large as 160% were found (Ding *et al* 2015).

3.3. Personalized patient dose

We reported the evaluated *CF* coefficients, for the selected scan and tube voltages, in table 5. These values were used for converting simulated dose, evaluated in mSv per photon, to dose to the patient model for the specific exam, in mSv per mAs.

For the female and male adult head phantoms provided by NCI, we calculated the dose for specific examinations whose characteristics were those evaluated for the Astelion CT scanner and previously reported. The scanning was performed with 4×1 beam aperture and for all the available tube voltages. This same scanner protocol was adopted for the computation of *CF* factors. Subsequently, we modified the standard female and male head phantoms in order to match the evaluated silhouette for two head manikins, representing actual patients head phantoms, as described in section 2.3. Differences in dose, evaluated for standard male adult head phantom and that evaluated for corresponding customized phantom,are reported in table 6.

Dose differences were evaluated for four selected tissues comprised in the head phantom: brain, eyeballs, eye lens and pituitary gland. The maximum difference was evaluated for lens dose at 135 kV (−13.7%). The customization of the male digital phantom on the basis of the measured silhouette, produced dimensions reductions of standard phantom of 13% in antero-posterior direction, and of 12% in lateral direction; in axial direction the standard phantom was extended by 8% to have the same length of the measured silhouette. The volume of the resulting head phantom was 18% smaller than the starting one. Similarly, dose differences evaluated for the female phantom are reported in table 7. In this case, the maximum discrepancy reached 38.0% for pituitary gland dose at 100 kV. These larger discrepancies may be ascribed to the stronger deformation to which the female standard digital phantom underwent. Indeed, to present the same dimensions of the measured

Table 8. Percentage dose discrepancies calculated via NCICT 3.0 software for the male phantom with a height of 175 cm and weight of 135 kg, with respect to the dose for 75 kg weight.

Tube voltage (kV)	Brain	Eyeballs	Eye lens	Pituitary gland
80	−0.3	−6.7	−8.9	0.8
100	−0.6	−6.2	−7.4	0.7
120	−0.3	−5.7	−7.5	0.6
135	−0.4	−5.8	−7.5	0.5

Table 9. Percentage dose discrepancies calculated via NCICT 3.0 software for the female phantom with a weight of 160 cm and weight of 125 kg, with respect to the dose for 70 kg weight.

Tube voltage (kV)	Brain	Eyeballs	Eye lens	Pituitary gland
80	2.6	−3.3	−7.5	0.2
100	2.1	−3.0	−7.5	−1.5
120	1.7	−3.0	−7.3	−0.5
135	1.8	−3.0	−7.3	−0.3

silhouette, the standard phantom was reduced by 26% in lateral direction, by 11% in antero-posterior direction and by 16% in axial direction, with a resulting volume reduction of 45%.

Tables 8 and 9 report dose discrepancies evaluated with NCICT 3.0 software in the case of customization of the patient model based on its weight. The adopted scanning protocol was the same used in previous tests. For a male phantom of 175 cm height, increasing the weight from 75 kg to 135 kg determined a maximum dose difference of 8.9%, evaluated for the eye lens. In the case of the brain dose, the discrepancies were less than 1.0% (table 8). The same test was performed for female phantoms of 160 cm height, and discrepancies were reported in table 9. In this case, the model weight was increased from 70 kg to as much as 125 kg, and the related discrepancies ranged between 2.6% and −7.5%, evaluated for the brain and the eye lens, respectively, at 80 kV.

4. Discussion

Evaluation of radiation dose in CT is a topic of high interest due to the increasing use of CT examinations worldwide and the corresponding dose burden. In a CT scan the organ dose mainly depends on patient's anatomy, scan region and scanner output; organ dose estimates permit to compute the effective dose for the given CT scan. However, the dose to the organs is not an immediate information, and the general approach is to use a Monte Carlo algorithm associated with an anthropomorphic phantom to calculate it. To date, several software programs have been introduced to calculate the organ dose in CT (e.g., CTExpo, National Cancer Institute CT, NCICTX, NEXO[DOSE]®, Virtual Dose). All these softwares allow to calculate a reference dose for standard phantoms or to evaluate the dose after the CT scan. We have proposed a personalized dose evaluation through a MC code and a customized phantom to evaluate a personalized dose estimate before the CT exam. This code is based on the phantom customization, realized through the adaptation of internal part of NCICT standard phantoms, to the external body silhouette derived from an optical 3D scan. The MC code was validated on a specific multi-detector spiral CT scanner (Toshiba Astelion), but it can be promptly adapted to replicate the characteristics of any clinical scanner. Our Geant4 based MC code for head CT simulation featured a processing time in the order of 4×10^5 primary photon histories s^{-1}, when running on a cluster of 128 processors on a multi-CPU server platform.

We point out that, in a recent work, we have demonstrated Graphics Processing Unit (GPU) accelerated fast MC simulations for processing times in the order of 10^9 photon histories s^{-1} (Mettivier *et al* 2022), with a code running on a single NVIDIA GeForce RTX 3090 GPU card (10496 NVIDIA CUDA cores, 24 GB GDDR6X RAM). This GPU code (initially developed by, and in collaboration with, the group of Prof X Jia at University Texas Southwestern) was intended for dedicated cone-beam breast CT, digital mammography, and digital breast tomosynthesis imaging and dosimetry. It includes a 3D dose map output (voxel resolution about 0.03 mm^3), as well as projection and tomographic imaging output, with a resolution in the order of $(0.3\ mm)^3$ for a phantom volume in the order of $10^6\ mm^3$. When translated to the head geometry and the helical simulation scheme used in this work, the adoption of this GPU-based MC code is expected to feature a total processing time in the order

of 10 s for dosimetry with statistical uncertainty less than a few percent. This predicted performance, still to be demonstrated for whole-body CT scans, would show the potential for the clinical implementation of the present approach for real-time pre-exam personalized organ dose estimates in multi detector CT. Tube current modulation (TCM) during the patient scan can be included in the MC code once the tube modulation function of the specific scanner type has been determined (e.g. retrospectively from archive scans by analyzing DICOM header's TCM info).

4.1. Code validation

The validation of the proposed code was realized by a comparison of simulated and measured beam profiles and CTDI. The Astelion CT scanner produced by Toshiba (model CGS-61A) was replicated in the code, and the beam was modelled using the HVL evaluate at the scanner isocenter. The hypothesis of beam uniformity in the axial direction was verified by radiochromic film measurements. We compared the simulated and measured beam profile evaluated as air-kerma normalized to the value at the isocenter, obtaining a discrepancy well below 1%. On the other hand, the comparison of simulated and measured $CTDI_w$, shows an absolute difference of 4% (figure 9), which is in line with, if not better than, values reported in the literature (Kostou *et al* 2019).

4.2. NCICT Validation

The dose values for brain, eyeballs, lens and pituitary gland, provided by our MC code using an NCI head phantom, showed a maximum discrepancy for the pituitary gland at 80 kV in the case of the male phantom (23.9%), and for lens dose at 135 kV in the case of the female phantom (24.8%), when compared to the calculation perfomed via the NCICT software (Lee *et al* 2015). In the other cases the differences were lower than 15%, in absolute value (tables 4 and 5). For comparison, these results are in complete agreement with the data reported in De Mattia *et al* (2020), where four different software codes used for organ dose estimates (CTExpo, NCICT, NCICTX, NEXO[DOSE]® and Virtual Dose) were tested, as well as with data from Samei *et al* (2020), where the evaluation of the different sources of uncertainty were analyzed.

4.3. Personalized patient dose

The developed MC code provided organ dose estimates using a customized phantom, realized through the adaptation of internal part of NCICT standard phantoms to the external body silhouette derived from an optical 3D scan. In the case of the male head phantom (table 6), where the phantom deformation led to a phantom's volume increase by 14%, the dose to the standard phantom was up to 14% higher than that evaluated for the customized phantom. The maximum differences were observed for the lens dose, with overestimations of customized phantoms ranging between 10.2% at 80 kV, and 13.7% at 135 kV. The lower differences were observed for the brain, not exceeding 5.1% in absolute value.

The head phantom modification in the case of the female individual (table 7) produced an overall increase of the volume by 31%. The volume modification observed, larger than that for the male phantom, may be the main cause of the larger observed discrepancies between dose evaluated for the standard and customized phantoms. Hence, the former led to dose estimates down to 38.0% lower than the second (evaluated for the pituitary gland at 100 kV). For the brain, the standard phantom underestimation ranged between 17.9% and 36.3%; these values ranged between 8.9% and 30.8% in the case of dose to the eyeballs, and 3.0% and 28.2% in the case of lens dose.

Moore *et al* (2014) proposed to customize the pediatric organ dose on the basis of the size specific dose estimates (AAPM 2011). Estimated values were within $\pm$10% compared to measurements with pediatric phantoms. More sophisticated models for body deformations have been adopted for dose re-evaluation in image guided radiotherapy (Brock *et al* 2017, Paganelli *et al* 2018) with the maximum dimensionality of the transformations reaching up to 3 times the number of the voxels contained in the image. Such deformations permitted to recalculate delivered doses to the organs with the purpose of keeping target doses unchanged after patient modification and repositioning.

The NCICT 3.0 softtware (Lee *et al* 2015), here adopted for our code validation,permits to customize the model of the patient in CT. In particular, it permits to manually input the height and the weight of the patient in order to select the most appropriate model over 370 digital phantoms representing both genders, children and adults. In a test performed in this paper, we considered two adult models, one for each gender, and evaluted the dose discrepancy obtained for the extreme of the allowed weight ranges, for a fixed model height. It is expected that such a weight range covers the maximum modification in silhouette for the selected phantoms, as well as the maximum dose discrepancies. In the case of the selected 175cm height male phantoms, going from 75 to 135 kg in weight does not produce substantial changes in absorbed dose, with maximum observed differences lower than 8.9% for eye lens at 80 kV. The customization proposed in this work, based on the measurement of the patient silhoutte, produced a difference of 13.7% for the same tissue, at 135 kV. In the case of 160cm female

model—where the customization based on the measured silhouette led to dose differences up to 38.0% evaluated for pituitary gland—going from 70 kg to 120 kg model weight produced a dose discrepancy less than 7.5%, for the considered head tissues.

The results here presented for personalized CT head scans will be extended to (more complex) anatomical districts: preliminary data (shown in figure S1 in Supplementary material), implementing the MC code for CT chest scans, were considered promising in view of the application of the proposed methodology to pre-scan organ dose estimates in routine clinical CT scans of all anatomical districts. We point out that in the application of the proposed methodology, once a whole-body 3D optical scan is derived for the fist time for a given patient, the personalized phantom could be used, also with the same or different MC codes, for organ dose estimates, in successive exams.

We also envisage the possibility of adopting the proposed 3D optical scan of the patient body for nuclear medicine personalized dosimetry with MC codes (e.g. Frezza *et al* 2020, Peng *et al* 2022) and for MC dosimetry in interventional radiology (e.g. Fum *et al* 2021, Fernández-Bosman *et al* 2022).

We are aware that presently, a limitation of this work—though not affecting the rationale of the new dosimetric method proposed—is related to the customization of the standard patient model to the silhouette of the actual one. Indeed, the adopted rigid adaptation scheme, based on the compression/stretching of the voxel sizes in the three spatial directions, may cause a deformation of those internal structures of the body which does not follow this proportional law (e.g. the eyballs, for the head phantom). In addition, deformation may also be caused by the presence of fat layers manly located in the outer borders of the body, causing a radiation shield effect and a dose reduction to the inner radiosensitive tissues. Application or development of more efficient deformable image registration methods should be investigated (e.g. Zvereva *et al* 2017, Borbinha *et al* 2019); moreover, the proposed methodology for personalized CT dosimetry should be compared to other approaches, as here done versus NCI tools for both the reference phantoms dataset and the organ dose estimate algorithm.

5. Conclusions

We carried out a validation of a new method for obtaining Monte Carlo-based personalized dose estimates in CT before performing the scan, which involves (i) to input a realistic patient body shape and size by 3D optical scanning, (ii) to compute a personalized voxelized body phantom by adaptation of reference phantoms, and (iii) to derive organ doses using a validated MC simulation. The proof-of-principle test shown here was conducted on adult head phantoms, with head organ dose estimates comparable with corresponding values obtained using reference body and organ phantoms provided by NIH/NCI dosimetry tool. Possible extension of the MC code to chest spiral CT scan was indicated.

Acknowledgments

We thank Dr Choonsik Lee (NIH/NCI) for kindly making available the NCI tools for CT dosimetry adopted in this work. We thank Dr Carmine Botta e Dr Luigi Urraro (Dipartimento di Scienze Biomediche Avanzate, Università di Napoli Federico II) for their help during the measurements with the clinical CT scanner. This work was supported by INFN, Italy, via the project MC-INFN.

Data availability statement

All data that support the findings of this study are included within the article (and any supplementary information files). Data will be available from 22 February 2023.

ORCID iDs

Antonio Sarno https://orcid.org/0000-0002-3034-7166
Giovanni Mettivier https://orcid.org/0000-0001-6606-4304
Antonio Varallo https://orcid.org/0000-0001-6279-6719
Paolo Russo https://orcid.org/0000-0001-9409-0008

References

AAPM 2011 *Size-Specific Dose Estimates (SSDE) in Pediatric and Adult Body CT Examinations (2011)* Report No 204 American Association of Physicists in Medicine, Alexandria VA (https://doi.org/10.37206/143)

AAPM 2019a *Estimating patient organ dose with computed tomography: a review of present methodology and required DICOM information.* Report No-246 American Association of Physicists in Medicine, Alexandria VA (https://doi.org/10.37206/190)
AAPM 2019b *Size specific dose estimate (SSDE) for head CT.* Report no-293 American Association of Physicists in Medicine, Alexandria VA (https://doi.org/10.37206/185)
Abuhaimed A and Martin C J 2020 Estimation of size-specific dose estimates (SSDE) for paediatric and adults patients based on a single slice *Phys. Med.* **74** 30–9
Borbinha J, Di Maria S, Madeira P, Belchior A, Baptista M and Vaz P 2019 Increasing organ dose accuracy through voxel phantom organ matching with individual patient anatomy *Radiat. Phys. Chem.* **159** 35–46
Brock K K, Mutic S, McNutt T R, Li H and Kessler M L 2017 Use of image registration and fusion algorithms and techniques in radiotherapy: report of the AAPM radiation therapy committee task group *Med. Phys.* **44** e43–76
Damilakis J 2021 CT dosimetry: what has been achieved and what remains to be done *Invest. Radiol.* **56** 62–8
De Mattia C, Campanaro F, Rottoli F, Colombo P E, Pola A, Vanzulli A and Torresin A 2020 Patient organ and effective dose estimation in CT: comparison of four software applications *Eur. Radiol. Exp.* **4** 14
Ding A *et al* 2015 VirtualDose: a software for reporting organ doses from CT for adult and pediatric patient *Phys. Med. Biol.* **60** 5601–25
di Franco F, Sarno A, Mettivier G, Hernandez A M, Bliznakova K, Boone J M and Russo P 2020 GEANT4 Monte Carlo simulations for virtual clinical trials in breast x-ray imaging: proof of concept *Phys. Med.* **74** 133–42
Einstein A J 2020 Medical radiation exposure to the U.S. population: the turning tide *Radiology* **295** 428–9
Fernández-Bosman D, von Barnekow A, Dabin J, Malchair F, Vanhavere F, Duch M A and Ginjaume M 2022 Validation of organ dose calculations with PyMCGPU-IR in realistic interventional set-ups *Phys. Med.* **93** 29–37
Frezza A, Joachim-Paquet C, Chauvin M and Després P 2020 Validation of irtGPUMCD, a GPU-based Monte Carlo internal dosimetry framework for radionuclide therapy *Phys. Med.* **73** 95–104
Fujii K, Nomura K, Muramatsu Y, Obara S, Ota H and Tsukagoshi S 2020 Correlation analysis of organ doses determined by Monte Carlo simulation with dose metrics for patients undergoing chest-abdomen-pelvis CT examinations *Phys. Med.* **77** 1–9
Fum W K S, Wong J H D and Tan L K 2021 Monte Carlo-based patient internal dosimetry in fluoroscopy-guided interventional procedures: a review *Phys. Med.* **84** 228–40
Geyer A M, O'Reilly S, Lee C, Long D J and Bolch W E 2014 The UF/NCI family of hybrid computational phantoms representing the current US population of male and female children, adolescents, and adults—application to CT dosimetry *Phys. Med. Biol.* **59** 5225–42
Hernandez A M, Seibert J A, Nosratieh A and Boone J M 2017 Generation and analysis of clinically relevant breast imaging x-ray spectra *Med. Phys.* **44** 2148–60
Huda W, Lieberman K A, Chang J and Roskopf M L 2004 Patient size and x-ray technique factors in head computed tomography examinations: I. Radiation doses *Med. Phys.* **31** 588–94
ICRP 2007 The 2007 recommendations of the international commission on radiological protection. ICRP publication 103 *Ann. ICRP* **37** 1–332
ICRP 2009 Adult reference computational phantoms. ICRP publication 110 *Ann. ICRP* **39** 1–164
ICRP 2020 Adult mesh-type reference computational phantoms. ICRP Publication 145 *Ann. ICRP* **49** 13–201
Kostou T, Papadimitroulas P, Papaconstadopoulos P, Devic S, Seuntjens J and Kagadis C G 2019 Size-specific dose estimations for pediatric chest, abdomen/pelvis and head CT scans with the use of GATE *Phys. Med.* **65** 181–90
Lee C, Kim K P, Bolch W E, Moroz B E and Folio L 2015 NCICT: a computational solution to estimate organ doses for pediatric and adult patients undergoing CT scans *J. Radiol. Prot.* **35** 891–909
Lee H *et al* 2019 Percentile-specific computational phantoms constructed from ICRP mesh-type reference computational phantoms (MRCPs) *Phys. Med. Biol.* **64** 045005
Li X, Samei E, Segars W P, Sturgeon G M, Colsher J G, Toncheva G, Yoshizumi T T and Frush D P 2011 Patient-specific radiation dose and cancer risk estimation in CT: I. Development and validation of a Monte Carlo program *Med. Phys.* **38** 397–407
Di Lillo F, Mettivier G, Sarno A, Tromba G, Tomic N, Devic S and Russo P 2016 Energy dependent calibration of XR-QA2 radiochromic film with monochromatic and polychromatic x-ray beams *Med. Phys.* **43** 583–8
Martin C J, Harrison J D and Rehani M M 2020 Effective dose from radiation exposure in medicine: past, present, and future *Phys. Med.* **79** 87–92
Mettivier G *et al* 2022 Virtual clinical trials in 2D and3D x-ray breat imaging and sosimetry: comparison of CPU-based and GPU-based monte carlo codes *Cancers* **14** 1027
Mettler F A *et al* 2020 Patient exposure from radiologic and nuclear medicine procedures in the united states: procedure volume and effective dose for the period 2006–2016 *Radiology* **295** 418–27
Moore B M, Brady S L, Mirro A E and Kaufman R A 2014 Size-specific dose estimate (SSDE) provides a simple method to calculate organ dose for pediatric CT examinations *Med. Phys.* **41** 071917
2019 National Council on Radiation Protection and Measurements *Medical Radiation Exposure of Patients in the United States NCRP Report*184Bethesda, MD: National Council on Radiation Protection and Measurements https://ncrponline.org/shop/reports/report-no-184-medical-radiation-exposure-of-patients-in-the-united-states-2019/
Paganelli C, Meschini G, Molinelli S, Riboldi M and Baroni G 2018 Patient-specific validation of deformable image registration in radiation therapy: overview and caveats *Med. Phys.* **45** e908–22
Papadakis A E and Damilakis J 2022 Assessment of abdominal organ dose from and image quality in varying arc trajectory interventional C-arm cobe beam CT *Phys. Med.* **102** 46–54
Peng Z *et al* 2022 Development of a GPU-accelerated Monte Carlo dose calculation module for nuclear medicine, ARCHER-NM: demonstration for a PET/CT imaging procedure *Phys. Med. Biol.* **67** 06NT02
Sahbaee P, Segars W P and Samei E 2014 Patient-based estimation of organ dose for a population of 58 adult patients across 13 protocol categories *Med. Phys.* **41** 072104
Samei E, Ria F, Tian X and Segars W 2020 A database of 40 patient-based computational models for benchmarking organ dose estimates in CT *Med. Phys.* **47** 6562–6
Sapignoli S, Roggio A, Boschini A, Guida F, Merlo C, Paiusco M, Zorz A and De Monte F 2022 Size-specific dose estimates for pediatric head CT protocols based on the AAPM report TG-293 *Phys. Med.* **100** 26–30
Sarno A, Dance D R, Van Engen R E, Young K C, Russo P, Di Lillo F, Mettivier G, Blisnakova K, Fei B and Sechopoulos I 2017a A Monte Carlo model for mean glandular dose evaluation in spot compression mammography *Med. Phys.* **44** 3848–60
Sarno A, Masi M, Antonelli N, Di Lillo F, Mettivier G, Castriconi R and Russo P 2017b Dose volume distribution in digital breast tomosynthesis: a phantom study *IEEE Trans. Radiat. Plasma Med. Sci.* **1** 322–8

Sarno A, Mettivier G, Bliznakova K, Hernandez A M, Boone J M and Russo P 2022 Comparisons of glandular breast dose between digital mammography, tomosynthesis and breast CT based on anthropomorphic patient-derived breast phantoms *Phys. Med.* **97** 50–8

Sarno A, Mettivier G, Di Lillo F, Bliznakova K, Sechopoulos I and Russo P 2018 Homogeneous vs patient specific breast models for Monte Carlo evaluation of mean glandular dose in mammography *Phys. Med.* **51** 56–63

Tomic N, Devic S, DeBlois F and Seuntjens J 2010 Reference radiochromic film dosimetry in kilovoltage photon beams during CBCT image acquisition *Med. Phys.* **37** 1083–92

Tsalafoutas I A, Harita M H, Al-Naemi H Y and Kalra M K 2020 Radiation dose monitoring in computed tomography: Status, options and limitations *Phys. Med.* **79** 1–15

Turner A C *et al* 2009 A method to generate equivalent energy spectra and filtration models based on measurement for multidetector CT Monte Carlo dosimetry simulations *Med. Phys.* **36** 2154–64

Turner A C *et al* 2010 The feasibility of a scanner-independent technique to estimate organ dose from MDCT scans: using CTDIvol to account for differences between scanners *Med. Phys.* **37** 1816–25

Valero C, Sarno A, Cutaia C, Poli M, Isoardi P and Stasi M 2022 On the suitability of XR-SP2 gafchromic films for dosimetry in mammography *Radiat. Phys. Chem.* **197** 110154

Zvereva A, Schlattl H, Zankl M, Becker J, Petoussi-Henss N, Yeom Y S, Kim C H, Hoeschen C and Parodi K 2017 Feasibility of reducing differences in estimated doses in nuclear medicine between a patient-specific and a reference phantom *Phys. Med.* **39** 100–12